PHYSICAL SCIENCES

Laser-scribed conductive, photoactive transition metal oxide on soft elastomers for Janus on-skin electronics and soft actuators

Ganggang Zhao[1]†, Yun Ling[1]†, Yajuan Su[2], Zanyu Chen[1], Cherian J. Mathai[3], Ogheneobarome Emeje[4], Alexander Brown[5], Dinesh Reddy Alla[6], Jie Huang[6], Chansong Kim[7], Qian Chen[7], Xiaoqing He[1,8], David Stalla[8], Yadong Xu[4], Zehua Chen[4], Pai-Yen Chen[9], Shubhra Gangopadhyay[3], Jingwei Xie[2], Zheng Yan[1,4]*

Laser-assisted fabrication of conductive materials on flexible substrates has attracted intense interests because of its simplicity, easy customization, and broad applications. However, it remains challenging to achieve laser scribing of conductive materials on tissue-like soft elastomers, which can serve as the basis to construct bioelectronics and soft actuators. Here, we report laser scribing of metallic conductive, photoactive transition metal oxide (molybdenum dioxide) on soft elastomers, coated with molybdenum chloride precursors, under ambient conditions. Laser-scribed molybdenum dioxide (LSM) exhibits high electrical conductivity, biocompatibility, chemical stability, and compatibility with magnetic resonance imaging. In addition, LSM can be made on various substrates (polyimide, glass, and hair), showing high generality. Furthermore, LSM-based Janus on-skin electronics are developed to record information from human skin, human breath, and environments. Taking advantage of its outstanding photothermal effect, LSM-based soft actuators are developed to build light-driven reconfigurable three-dimensional architectures, reshapable airflow sensors, and smart robotic worms with bioelectronic sensors.

INTRODUCTION

Laser-assisted, mask-free fabrication is emerging as a versatile and powerful technique for the scalable production of conductive materials with customized patterns on flexible substrates (*1*–*5*). For example, laser-induced graphene (termed as LIG), taking advantage of laser irradiation–induced, localized, high temperatures to convert carbonaceous materials into porous graphene with arbitrary patterns under ambient conditions, features simple fabrication, easy customization, and high electrical conductivity and has shown promising applications in flexible electronics, soft actuators, artificial throats, energy storage, and others (*6*–*9*). Despite recent progresses in laser-assisted fabrication, it remains challenging to enable laser scribing of graphene or other highly conductive materials on tissue-like soft elastomers. For instance, high-quality LIG is usually obtained on rigid polyimide (PI) films (Young's modulus, ~2.5 GPa) (*1*), which has a big mechanical mismatch with biological tissues. Soft elastomers indicate tissue-like pliability, high stretchability, and biocompatibility. In addition, their integrations with customized conductive patterns are the ideal building blocks (e.g., conductive traces and basis electrodes) to make various biointerfaced electronics and soft actuators (*10*–*12*). While LIG can be transferred from rigid PI mother substrates onto soft elastomer substrates for bio-related applications, the additional transfer-printing process is complicated and tedious (*13*). It is worth noting that laser-assisted fabrication of silicon carbide (SiC) has been recently achieved on soft silicone elastomers (*14*, *15*). However, laser-scribed SiC demonstrates a relatively poor electrical conductivity, thereby restricting its broad applications in on-skin electronics and others.

Molybdenum dioxide (MoO_2) is an unusual and attractive transition metal oxide because of its metallic electrical resistivity (8.8×10^{-5} ohm·cm), high chemical stability, high biocompatibility, and low magnetic susceptibility (*16*–*18*), which is a fascinating material for bioelectronic applications. In addition, on account of its high photothermal conversion efficiency (more than 60% in the near-infrared region) (*19*, *20*), MoO_2 can be adopted for light-driven soft actuators. In the present, MoO_2 is mainly prepared using hydrothermal or calcination methods and is usually used for photothermal therapy, lithium-ion batteries, electrocatalysts, surface-enhanced Raman spectroscopy, and others (*18*, *21*–*23*). Even with these promising properties, the applications of MoO_2 in emerging bioelectronics and soft actuators are still rare, mainly because of the lack of the fabrication technique that can enable simple, scalable, and mask-free fabrication of MoO_2 on tissue-like soft elastomers under ambient conditions.

To fill the aforementioned gaps in material fabrications, here, we first demonstrate laser-assisted, mask-free, scalable scribing of MoO_2 (termed as LSM) on soft elastomers and other substrates under ambient conditions. In addition, existing on-skin wearables usually have bioelectronic devices patterned on the bottom side that directly touches human skin to record various biosignals (*9*, *10*). In addition, studies of developing Janus wearable devices, which have different biosensing functions on the skin-touch side and air-exposed side, are still rare. Here, we have further developed LSM-based Janus on-skin wearables with different bioelectronic devices patterned on the

[1]Department of Mechanical and Aerospace Engineering, University of Missouri, Columbia, MO, USA. [2]Department of Surgery-Transplant and Mary and Dick Holland Regenerative Medicine Program, University of Nebraska Medical Center, Omaha, NE, USA. [3]Department of Electrical Engineering and Computer Science, University of Missouri, Columbia, MO, USA. [4]Department of Biomedical, Biological and Chemical Engineering, University of Missouri, Columbia, MO, USA. [5]Cognitive Neuroscience Systems Core, University of Missouri, Columbia, MO, USA. [6]Department of Electrical and Computer Engineering, Missouri University of Science and Technology, Rolla, MO, USA. [7]Department of Materials Science and Engineering, University of Illinois at Urbana-Champaign, Urbana, IL, USA. [8]Electron Microscopy Core, University of Missouri, Columbia, MO, USA. [9]Department of Electrical and Computer Engineering, University of Illinois at Chicago, Chicago, IL, USA.
*Corresponding author. Email: yanzheng@missouri.edu
†These authors contributed equally to this work.

two sides, which can provide concurrent monitoring of comprehensive information from human skin, human breath, and environments for potential applications in health monitoring and daily-life management. Besides, soft actuators based on LIG have been recently achieved, which are usually electrothermally actuated and need conductive wires to connect soft actuators with external power sources (*12*). In this work, we have developed LSM-based, untethered, light-driven soft actuators and demonstrated their applications in reconfigurable three-dimensional (3D) architectures, reshapable wearable airflow sensors, and smart soft robotic worms with bioelectronic sensors.

RESULTS

Fabrication and characterization of laser-scribed MoO_2

The fabrication process of LSM is illustrated in Fig. 1A. Briefly, the process starts with spray coating of molybdenum chloride ($MoCl_5$) on supporting substrates, which are annealed at 85°C for 2 min in the air. Next, CO_2 laser irradiation is used to convert the precursors into MoO_2 under ambient conditions by a photothermal process. Here, CO_2 laser centers at 10.6 μm with a range of 927 to 951 cm^{-1} (*24*). These frequencies can be well absorbed by the precursors (fig. S1). The Hilbert serpentine pattern is used as an illustrative example, and the computer-controlled CO_2 laser beam can create arbitrary

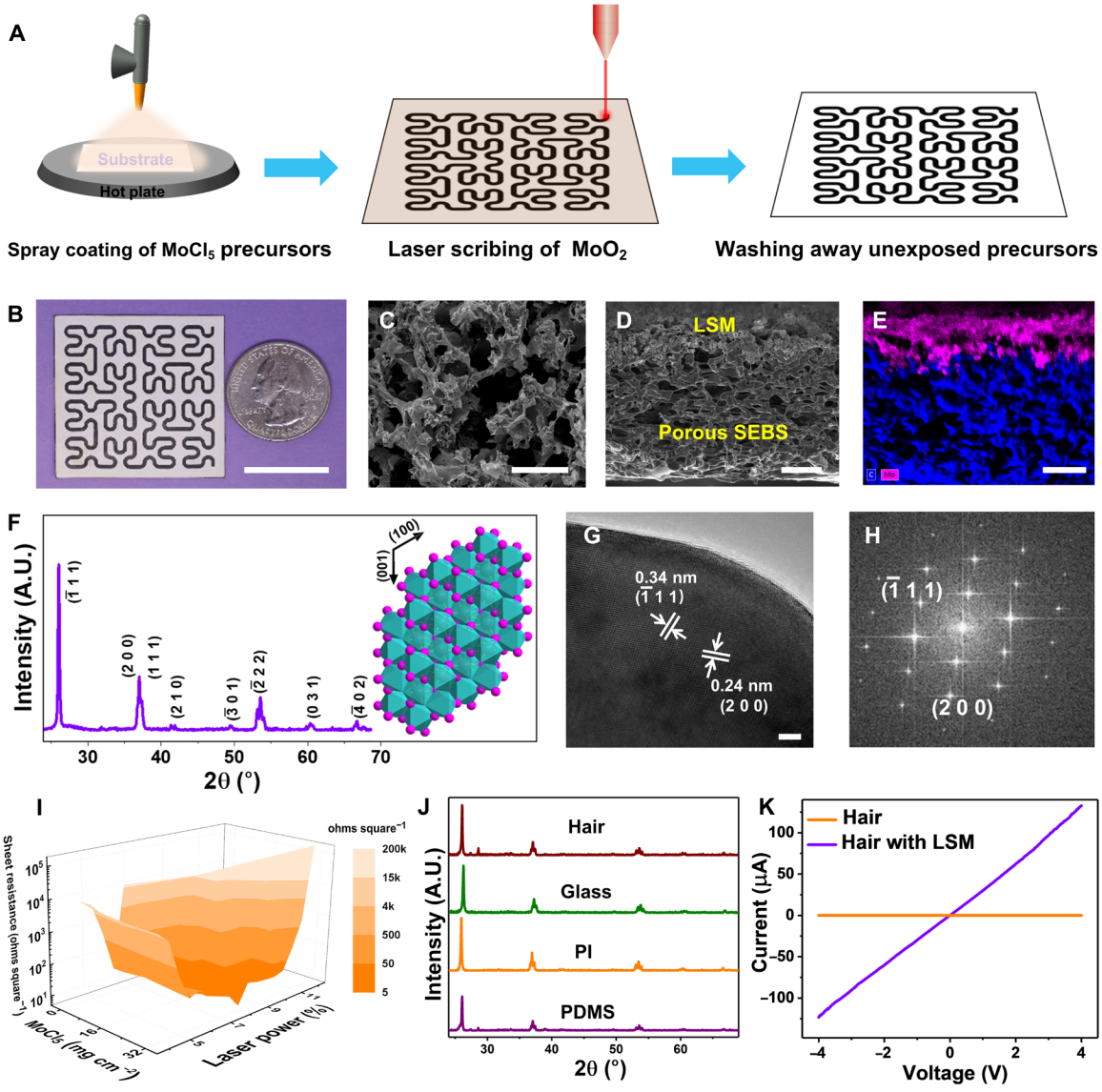

Fig. 1. Fabrication and characterization of laser-scribed MoO_2. (**A**) Schematic illustration of laser scribing of MoO_2 on supporting substrates. (**B**) Optical image of LSM with the Hilbert pattern on porous SEBS. Scale bar, 2 cm. Top-view SEM image (**C**), cross-sectional SEM image (**D**), and cross-sectional EDS mapping of Mo (pink) and C (blue) elements (**E**) of LSM on porous SEBS. Scale bars, 20 μm (C), 50 μm (D), and 50 μm (E). (**F**) XRD pattern of LSM on porous SEBS. Inset: Crystal structures of monoclinic MoO_2. A.U., arbitrary units. (**G** and **H**) HRTEM image and corresponding fast Fourier transform pattern of LSM. Scale bar, 5 nm. (**I**) Variation of sheet resistances of LSM on porous SEBS as a function of the laser-scribing power and the amount of spray-coated $MoCl_5$ precursors. The color bar indicates distributions of sheet resistances. (**J**) XRD patterns of LSM fabricated on human hair, glass, PI, and PDMS. (**K**) Current-voltage relation (*I-V*) curves of human hair before and after LSM fabrication.

MoO_2 patterns on substrates coated with precursors. In the end, washing away the precursors, unexposed to the CO_2 laser irradiation, completes the fabrication process. More details about LSM fabrication are provided in Materials and Methods.

Phase separation–synthesized porous poly(styrene-ethylene-butadiene-styrene) (SEBS) is used as the substrate example to illustrate LSM formation because of its ultrasoftness (Young's modulus, ~1.5 MPa), high breathability, and self-cooling effect (*25*), which is a promising soft supporting substrate for on-skin bioelectronics. Figure 1B provides an optical image of a laser-scribed Hilbert serpentine pattern of MoO_2 on porous SEBS. Figure S2 displays an array of LSM letters of laser-scribed MoO_2 on porous SEBS, indicating scalability and high reproducibility of the laser-assisted fabrication. The top-view scanning electron microscopy (SEM) image (Fig. 1C) demonstrates that LSM exhibits porous structures. The cross-sectional SEM image (Fig. 1D) and corresponding energy-dispersive x-ray spectroscopy (EDS) element mapping (Fig. 1E) show the interconnected interface of LSM and porous SEBS, and the thickness of LSM is ~50 μm. Furthermore, x-ray diffraction (XRD) analysis (Fig. 1F) shows that LSM can be indexed as the monoclinic-phase MoO_2 [Joint Committee on Powder Diffraction Standards (JCPDS), 32-0671] with lattice constants of a = 5.6068 Å, b = 4.8595 Å, and c = 5.5373 Å (*26*). The inset in Fig. 1F illustrates the crystal structure of MoO_2, where six O atoms form an octahedron with a Mo atom in the center, occupying half the space of the octahedron. All the O atoms in the octahedron are triply shared to form a monoclinic MoO_2, which is a distorted rutile structure with two alternative Mo—Mo bond distances, contributing to high electrical conductivity (*16*, *23*). The Raman spectrum of LSM (fig. S3) further confirms the formation of MoO_2. The characteristic peaks at ~571 and 744 cm^{-1} arise from Mo—O bond vibration modes, while other fingerprint peaks at ~201, 228, 361, 462, and 495 cm^{-1} can be attributed to phonon vibration modes of MoO_2 (*23*). The high-resolution transmission electron microscopy (HRTEM) image (Fig. 1G) and corresponding fast Fourier transform pattern (Fig. 1H) demonstrate that LSM has a high degree of crystallinity. The spacing of the lattice fringe of 0.34 and 0.24 nm can be indexed to $(\bar{1}11)$ and (200) planes of monoclinic MoO_2, respectively. Moreover, as shown in Fig. 1I, a low sheet resistance of ~4.6 ohms $square^{-1}$ can be achieved on LSM by optimizing the laser-scribing power and the amount of $MoCl_5$ precursors coated on porous SEBS, which is well suitable for bioelectronic applications. In addition, the laser-assisted fabrication process is highly repeatable, and an SD of 0.4 ohms $square^{-1}$ is obtained in the sheet resistances of 20 independently prepared LSM samples (fig. S4). It is worth noting that laser irradiation on porous SEBS without coating $MoCl_5$ precursors results in substrate ablation (fig. S5) instead of the formation of LIG, possibly due to its low melting point and lack of cross-linked aromatic structures (*27*). In addition to porous SEBS, LSM has been made on a variety of substrates, including polydimethylsiloxane (PDMS), PI, glass, and even human hair (Fig. 1J and figs. S6 and S7) using similar procedures, indicating high generality of the reported fabrication technique. Figure S7 provides an SEM image of LSM formed on human hair. After LSM formation, human hair becomes conductive (Fig. 1K). In addition, as shown in fig. S8, LSM indicates high stability at high temperatures and in both strong acid and strong alkali. In addition, as shown in fig. S9, with precursor coating, laser irradiation has small effects on the underneath polymer substrates during MoO_2 fabrication, possibly due to the strong absorptions of precursor materials in the CO_2 laser wavelengths (fig. S1A). Notably, LSM fabrication has a negligible effect on the breathability (water vapor transmission) of the porous elastomer substrate (fig. S10) owing to the porous structures of LSM and well-preserved porous structures of porous SEBS after LSM fabrication (fig. S9).

In addition, cytotoxicity tests were conducted by incubating three different types of cell lines, including human immortalized epidermal cells (HaCaT), human histiocytic lymphoma cells (U937), and human dermal fibroblasts (HDF-α), on LSM. Here, the obtained data were evaluated for statistical significance using an ordinary two-way analysis of variance (ANOVA) followed by Tukey's post hoc multiple comparison test, and the differences were considered significant at $P < 0.05$. The relative fluorescence intensity (Fig. 2A) shows that there are no significant differences ($P > 0.05$) in cell viability among the cells cultured with LSM and on tissue culture polystyrene (control) on the fifth day. The fluorescence micrographs (Fig. 2B) show that HaCaT cells attach well and spread uniformly on LSM, and no visible (VIS) apoptosis or necrosis was observed, indicating outstanding biocompatibility. Besides, it is desirable to develop magnetic resonance imaging (MRI)–compatible bioelectronics (*28*, *29*). The unique combination of MRI and bioelectronics can provide comprehensive information of the human psychological state. Here, the magnetic susceptibility of LSM is about −2 parts per million (ppm) (Fig. 2C). The material is usually considered to be MRI compatible when the absolute value of the magnetic susceptibility difference between the investigated material and water (magnetic susceptibility, −9 ppm) is less than 10 ppm (*30*). As shown in Fig. 2D, LSM has better MRI compatibility than several other conductive materials used in bioelectronics [e.g., platinum (Pt), gold (Au), and silver (Ag)] (*30*). While copper (Cu) has better MRI compatibility than LSM, Cu can be easily oxidized into copper oxide with high magnetic susceptibility (~17 ppm) (*31*) in the air and biofluids, dampening its promise. In addition, a negligible temperature fluctuation was observed on LSM during a 20-min MRI scanning process (Fig. 2E), measured with a fiber optic temperature sensor. To further demonstrate MRI compatibility, LSM was attached on a porcine head (fig. S11) for imaging using a 3T clinical MRI scanner. The obtained MRI images show no artifacts or distortion in the LSM vicinity [obtained from T1-weighted magnetization prepared rapid acquisition gradient echo (MPRAGE) sequence scans and T2-weighted sampling perfection with application optimized contrasts using different flip angle evolution (SPACE) sequence scans, respectively; Fig. 2F and fig. S12], indicating outstanding MRI compatibility. Meanwhile, LSM fabricated on porous SEBS with kirigami cutting patterns exhibits promising flexibility, stretchability, and cyclability (fig. S13).

Janus on-skin wearables based on laser-scribed MoO_2

Emerging on-skin wearable electronics can provide continuous, real-time monitoring of a range of physiological signals from human skin and can find wide applications in human health care, fitness tracking, human-machine interface, and others (*32*–*34*). Despite the recent considerable progress, on-skin wearables with Janus device layouts, which can not only record multiple biological signals from human skin but also capture useful information from human breath and surrounding environments, are still rare. In this section, we have demonstrated the Janus on-skin wearables based on LSM patterned on porous SEBS (Fig. 3A). The top side (Fig. 3B and fig. S14A) of the Janus wearable is exposed to air and has the alcohol gas sensor, humidity sensor, ultraviolet (UV) sensor, and ammonia (NH_3) gas sensor, consisting of LSM interdigital electrodes coated with tungsten diselenide

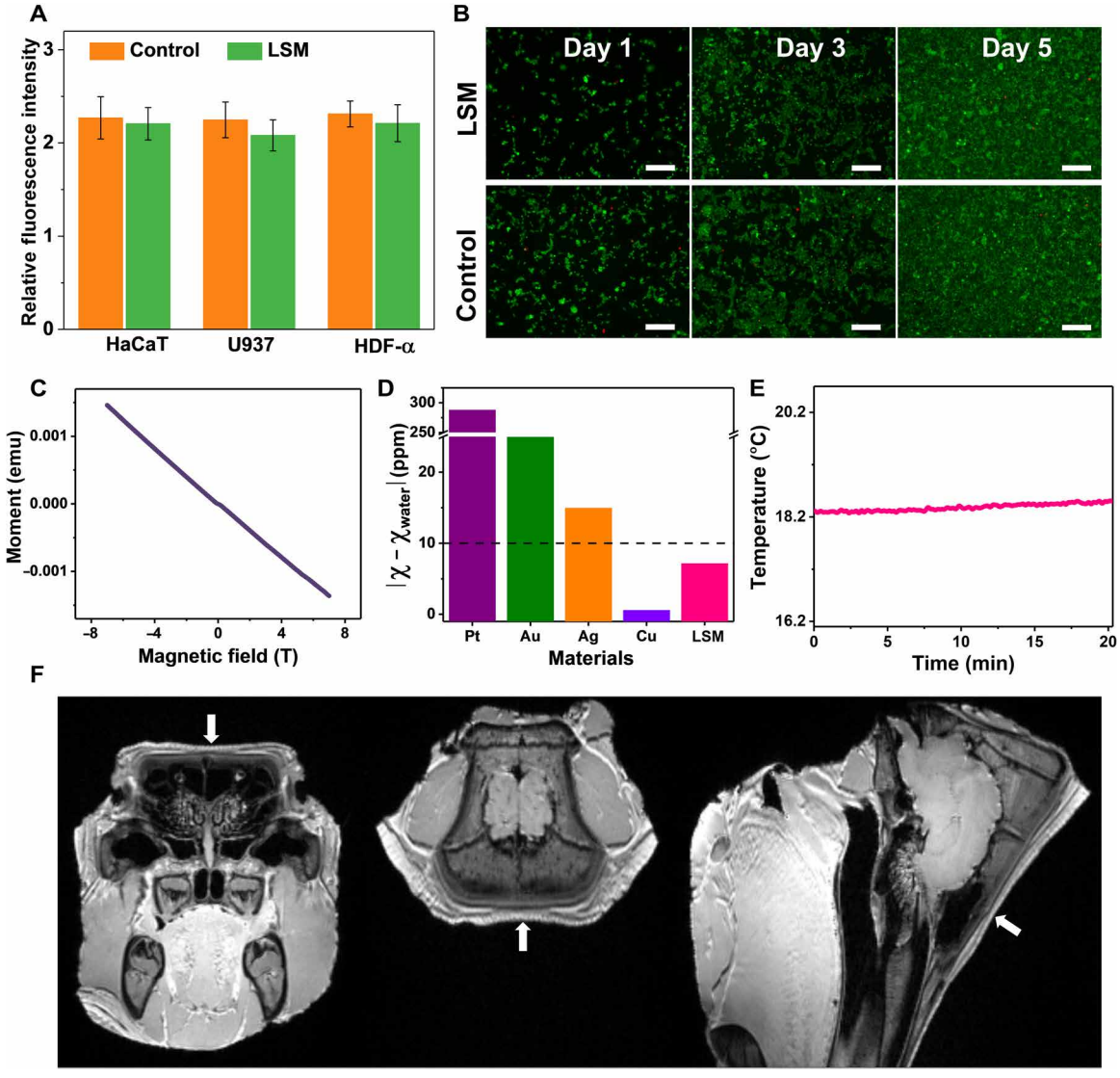

Fig. 2. Cytotoxicity tests and MRI compatibility characterization of laser-scribed MoO_2. (**A**) Relative fluorescence intensity of three cell lines after 5 days of culturing on the LSM and control sample (tissue culture polystyrene). (**B**) Fluorescence images of stained HaCaT cells on the LSM and control sample after 1, 3, and 5 days of culturing. Live and dead cells were stained in green and red, respectively. Scale bars, 50 μm. (**C**) Magnetic susceptibility of LSM on porous SEBS measured at 300 K under applied magnetic fields of −7 to 7 T. (**D**) Absolute values of magnetic susceptibility (χ) differences between water and some conductive materials (LSM, Pt, Au, Ag, and Cu) used in bioelectronics. (**E**) Temperature changes of LSM during the MRI scanning measured with a fiber optic temperature sensor, showing negligible fluctuation. MRI images of a porcine head attached with LSM from the coronal (left), axial (middle), and sagittal (right) directions (**F**), showing no distortion or artifact in the LSM vicinity. The arrows indicate the LSM location on the porcine head.

(WSe_2) nanoflakes, graphene oxides (GO), zinc oxide (ZnO) nanowires, and *p*-toluene sulfonate hexahydrate–doped polyaniline (PTS-PANI), respectively. The bottom side of the Janus wearable (Fig. 3C and fig. S14B) directly touches human skin and has the electrophysiological sensor, temperature sensor, and sweat biochemical sensor. The electrophysiological sensor consists of LSM reference, ground, and measurement electrodes, which can monitor electrocardiograms (ECGs), electroencephalograms (EEGs), and electromyograms (EMGs). The temperature sensor consists of an LSM conductive trace and can measure the body temperature. The sweat biochemical sensor consists of the LSM counter electrode, LSM working electrode (coated with carbon inks), LSM working electrode (coated with carbon inks, Au nanoparticles, Prussian blue, and glucose oxidase), and LSM reference electrode [coated with silver/silver chloride (Ag/AgCl)] and can concurrently measure glucose, uric acid (UA), and caffeine (CAF) from human sweat (fig. S15). Here, the sweat-sensing area is covered with the sweat absorption pad (Texwipe TX609) for sweat collection. Besides, gelatin-dopamine–based adhesives are coated on porous SEBS to improve the device stickiness and enhance the conformal contact between the Janus wearable and skin (Fig. 3D and fig. S16).

In addition, the Janus wearable device can be interfaced with the mobile data acquisition circuit (fig. S17) for in situ data processing and wireless data transmission by Bluetooth Low Energy. Here, the mobile data acquisition circuit is assembled on a flexible printed circuit board with the off-the-shelf electronic components (Fig. 3E). The simplified block diagram is shown in Fig. 3F, and the detailed

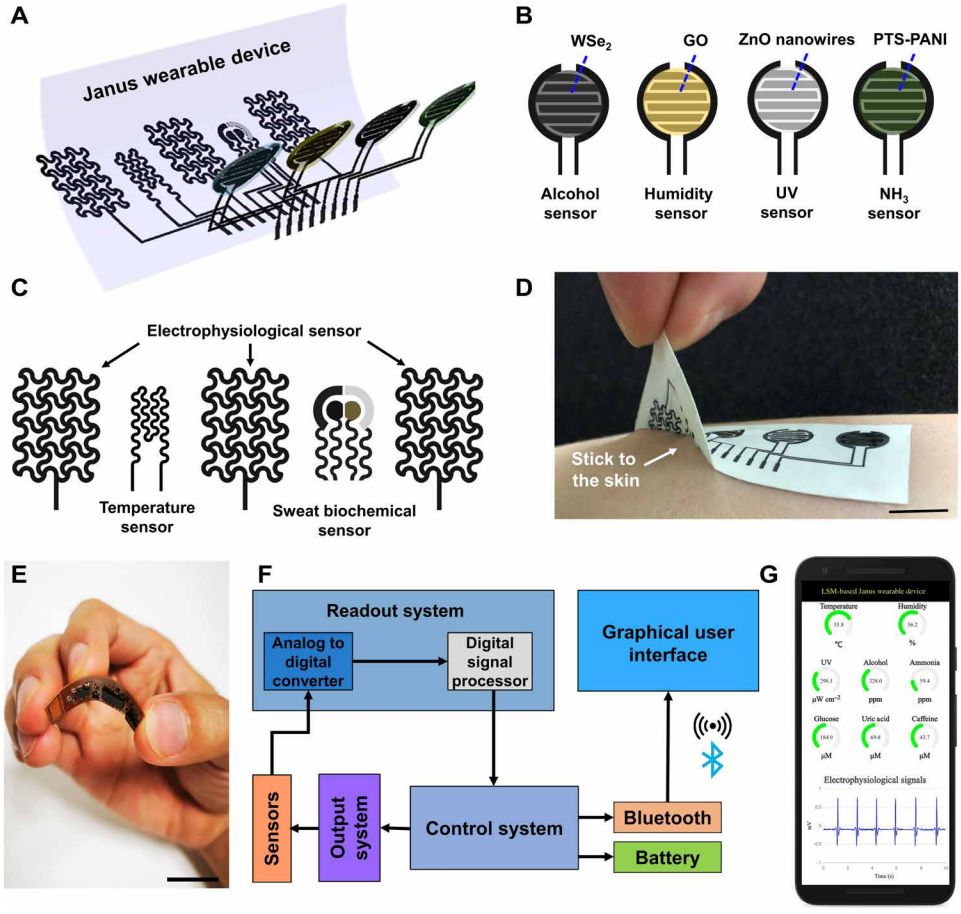

Fig. 3. Janus on-skin wearables based on laser-scribed MoO_2. (**A**) Exploded view of the Janus on-skin wearable based on LSM patterned on porous SEBS. Schematic illustration of bioelectronic devices on the top side (**B**) and the bottom side (**C**) of the Janus wearable. (**D**) Photograph showing the good stickiness between the Janus wearable and skin. (**E**) Photograph of the flexible printed circuit board assembled with off-the-shelf electronic components for in situ data processing and Bluetooth-enabled wireless data transmission. (**F**) System-level block diagram of the mobile data acquisition circuit. (**G**) Illustration of graphic data display on the smartphone installed with a customized software application. Scale bars, 1 cm. Details about the performance and characterization of LSM-based on-skin bioelectronic devices are provided in figs. S20 to S31. Mobile data acquisition, wireless data transmission, and graphic display on the smartphone are demonstrated in movie S1.

design and used off-the-shelf electronic components are provided in figs. S18 and S19 and table S1. In addition, the recorded biosignals can be displayed on the smartphone installed with a customized mobile software application (Fig. 3F and movie S1).

Figures S20 to S27 display the performance and characterization of representative LSM-based bioelectronic devices that touch the skin (i.e., devices on the bottom side of the Janus wearable). Here, the obtained LSM-based devices can monitor a rich variety of health-related biophysical and biochemical signals from human skin and can provide programmed thermal and electrical stimulations on human body. In specific, the LSM-based temperature sensor exhibits a positive temperature coefficient of resistance (0.72% $^{o}C^{-1}$) and can capture dynamic skin temperature changes after applying a hot pad (fig. S20, A to C). The same device can be used as a joule heater by applying voltages on the LSM conductive trace, which can operate well on the human wrist at the flexed and extended states (fig. S20, D and E). In addition, the LSM-based electrophysiological sensor, with the skin-device contact impedance comparable to that of conventional Ag/AgCl gel electrodes (fig. S21), can perform high-fidelity measurements of ECG, EEG, and EMG from various locations in the human body. Figure S22 (A and B) shows that the LSM-based electrophysiological sensor can continuously record ECG signals from the human chest with high quality (signal-to-noise ratio, ~21.2 dB) and clearly distinguishable P-wave, QRS complex, and T-wave. The respiration rates and instantaneous heart rates (HRs) can be determined from recorded ECG signals, and the results agree well with the data measured with conventional methods (fig. S22, C to E). In addition, the electrophysiological sensor can capture EEG signals from foreheads when human volunteers first opened their eyes for 50 s and then closed their eyes for 100 s (alpha rhythm with the frequency centered at ~10 Hz; fig. S23). In addition, distinguishable EMG signals (signal-to-noise ratio, ~19.2 dB) can be detected by the LSM-based electrophysiological sensor from the forearm (flexor carpi radialis muscle) when the volunteer bent his wrist for different times and bent his different fingers (fig. S24, A and B). Moreover, programmed electrical stimulations can be applied to human body using LSM-based electrodes. In addition, the stimulation signals and induced EMG signals (fig. S24C) recorded from the same muscle (flexor

carpi radialis muscle) align well with each other, indicating potential applications in wound healing, pain relief, and rehabilitation by providing programmed electrical stimulations (*35*–*37*).

Sweat biochemical sensing can provide insights into the health status from the molecular level (*38*, *39*). In this work, we have developed LSM-based sweat biochemical sensors for glucose, UA, and CAF detections (fig. S15), which can be further extended for monitoring other sweat biochemicals via additional functionalizations of LSM basis electrodes. The glucose detection is based on the glucose oxidation by the glucose oxidase on the LSM working electrode (coated with carbon inks, Au nanoparticles, Prussian blue, and glucose oxidase), which is accompanied with hydrogen peroxide production. The current produced by oxidizing hydrogen peroxide is linearly proportional to the glucose concentration. Thus, glucose concentrations can be determined by monitoring the response currents (sensitivity, ~15.7 nA μM^{-1}; fig. S25, A and B). In addition, fig. S25 (C to E) indicates that the LSM-based glucose sensor exhibits high repeatability, long-term stability, and high selectivity. For example, as shown in fig. S25E, the interferential sweat analytes of lactate, UA, and CAF have a negligible effect on glucose monitoring. UA and CAF detection is based on the electrochemical oxidations of UA and CAF under different specific potentials (UA, ~0.15 V; CAF, ~1.11 V) on LSM working electrodes (coated with carbon inks) using the differential pulse voltammetry method, demonstrating high sensitivity, repeatability, stability, and selectivity (figs. S26 and S27). For example, the produced currents of UA and CAF oxidations are linearly proportional to their concentrations with sensitivity at ~63.9 and ~47.3 nA μM^{-1}, respectively. In addition, interferential sweat analytes (glucose, lactate, CAF, or UA) have negligible effects on the detections of UA and CAF.

Figures S28 to S31 show the performance and characterization of LSM-based representative bioelectronic devices that are exposed to air (i.e., devices on the top side of the Janus wearable), which are useful in health and environmental monitoring. For example, excessive exposure to UV radiation has associated risks with various medical conditions (e.g., skin cancer and skin aging) (*40*). The fabricated UV sensor, consisting of LSM interdigital electrodes coated with ZnO nanowires, can detect UV light intensity (fig. S28) based on the photogenerated variations in the concentrations of the surface states on ZnO nanowires (*41*), indicating a large on/off ratio (~10^4) and a rapid response time (~22 s). In addition, the humidity in the air and human breath can be detected on the basis of the water absorption and desorption on GO (*42*) coated on the LSM interdigital electrode (fig. S29), which can lead to capacitance change. Besides, the alcohol gas sensor, consisting of LSM interdigital electrodes coated with WSe_2 nanoflakes, can detect alcohol gas concentrations in the human breath samples (fig. S30) because the absorbed alcohol molecules on WSe_2 can reduce the depletion layer formed by O_2 absorption, attributing to more electron release and leading to decreased resistance (*43*). Moreover, detecting amine gases (e.g., ammonia, putrescine, and cadaverine) can be achieved on the PTS-PANI–coated LSM interdigital electrodes because the amine groups of absorbed gas molecules can donate lone electrons to PTS-PANI, resulting in dedoping and increasing the resistance of PANI (*44*). As shown in fig. S31, the obtained NH_3 gas sensor can not only detect NH_3 concentrations in human breath samples, which is useful for some diseases diagnosis (e.g., liver failure) (*45*), but also respond to biogenic amine gases (e.g., putrescine and cadaverine) for monitoring food spoilage (*44*).

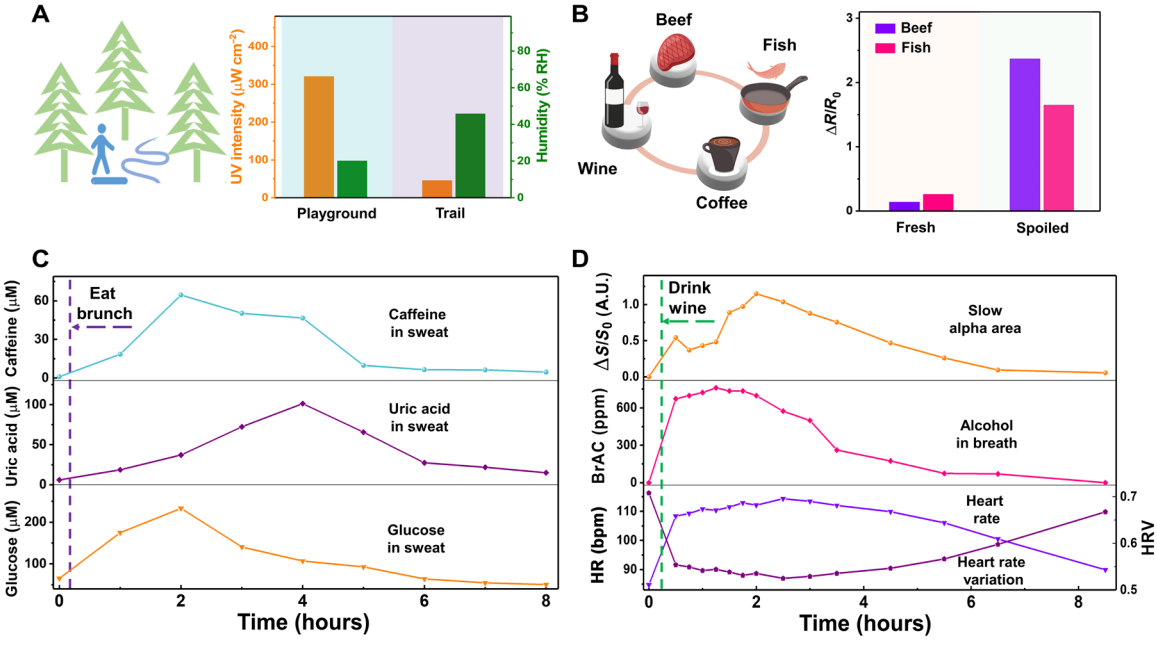

Fig. 4. Demonstration of LSM-based Janus on-skin wearables in daily-life activities. (**A**) Illustration (left) and the UV light density and relative humidity (RH) on the campus playground and a nearby trail (right) measured with the LSM-based Janus wearable. (**B**) Illustration (left) and electrical resistance responses of the LSM-based ammonia sensor to the fresh and spoiled fish and beef (right). (**C**) Dynamic concentration changes of the CAF, UA, and glucose in human sweat before and after eating brunch (including beef, fish, and coffee) over an 8-hour period. Here, exercise was used to produce sweat. (**D**) Dynamic changes of the relative changes of slow alpha area ($\Delta S/S_0$), breath alcohol concentration (BrAC), HR, and HRV before and after drinking wine [~0.5 g of white wine (56% alcohol by volume) per 1 kg of body weight of the human volunteer] over an 8.5-hour period. Here, all the experiments were repeated three times independently with similar results.

Demonstration of Janus on-skin wearables in daily-life activities

In addition to potential applications in health care enabled by physiological monitoring and programmed stimulations, we have further demonstrated the potential applications of LSM-based Janus wearables in daily activities (Fig. 4). In the first scenario, a human volunteer took a walk on the campus playground where high UV intensity (~321 μW cm^{-2}) and low relative humidity (~20%) were detected.

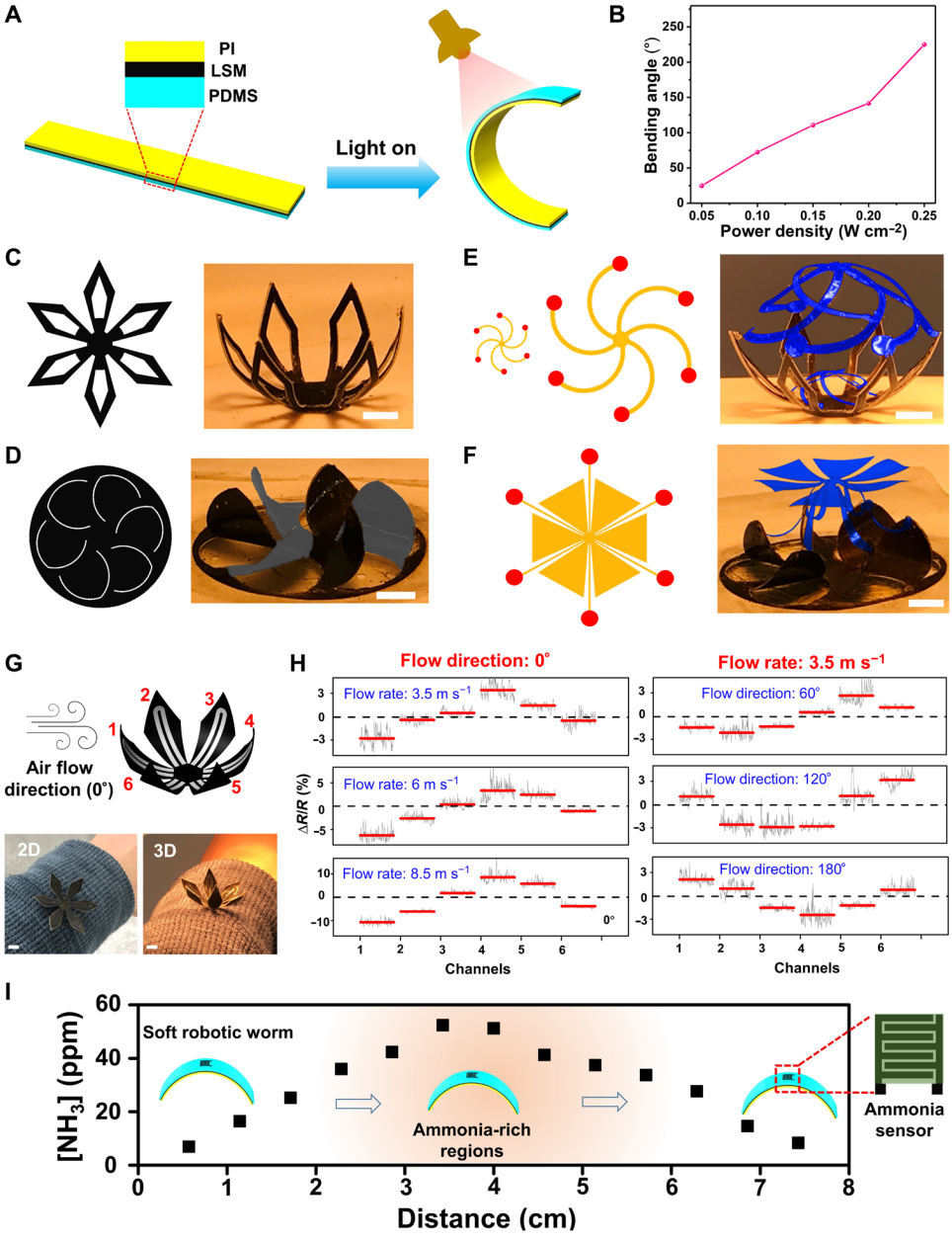

Fig. 5. LSM-based light-driven soft actuator and its applications in reconfigurable 3D structures, reshapable wearable devices, and soft robots. (**A**) Schematic illustration of LSM-based light-driven soft actuator. (**B**) Maximum bending angles of LSM-based soft actuator as a function of the power density of the infrared lamp (Phillips, BR40 Infrared Lamp). Flower-like (**C**) and windmill-like (**D**) reconfigurable 3D structures (right) and their corresponding 2D patterns (left). Reconfigurable multilayer 3D architectures (right) formed by combining LSM-based soft actuator with the mechanically assembled bilayer cage (**E**) and umbrella (**F**) and the corresponding 2D patterns of the cage and umbrella (left). Here, red dots in 2D patterns indicate bonding sites. (**G**) Schematic illustration and optical images of the reshapable wearable airflow sensor. The airflow sensor consists of six petal-like LSM soft actuators, and each of them is integrated with a strain gauge made of LIG, classified as sensing channels 1 to 6. Scale bars, 0.5 cm (C to G). (**H**) Electrical resistance responses of the six sensing channels of the reshapable airflow sensor under different flow rates (left) and flow directions (right). (**I**) Ammonia gas concentrations at different locations of a trail 8 cm in length, measured by a smart robotic worm integrated with an ammonia gas sensor. Here, an open bottle with the ammonium hydroxide solution (~30% by weight) was placed in the middle of the trail. In addition, the light-driven smart robotic worm moved from one end to the other end of the trail, guided by single-way stairs (*54*). Besides, recent research indicates that soft robotic worms with specific asymmetric structural designs can also perform one-way movement without needing single-way stairs (*55*, *56*).

Thus, the volunteer went to a nearby trail for a walk (Fig. 4A), which is surrounded by trees and a rivulet and has a healthy environment (UV intensity, ~45 μW cm^{-2}; humidity, ~45%). In the second scenario, the volunteer had beef, fish, and coffee for his brunch. Before cooking beef and fish, the volunteer checked the food spoilage using LSM-based Janus wearables (Fig. 4B). After finishing brunch, the glucose, UA, and CAF in the sweat of the volunteer were tracked using LSM-based Janus wearables. Figure 4C shows that the sweat concentrations of these biochemicals first markedly increased and then returned to their normal levels after about 8 hours due to metabolism. In the second day, the volunteer drank white wine [~0.5 g of white wine (56% alcohol by volume) per 1 kg of body weight of the volunteer]. It is known that alcohol intake has both short-term and long-term effects on the human body and behavior. Here, LSM-based Janus wearables can track the brain and heart activities and breath alcohol concentrations of the volunteer (Fig. 4D), showing potential applications in alcoholism studies. In specific, slow alpha activity ($\Delta S/S_0$) rapidly increased at the beginning 15 min of wine drinking, associated with episodes of subjective euphoria caused by alcohol intake, and then relatively slowly increased to the peak value in the following 2 hours, consistent with a more relaxed but awake mental state induced by alcohol intake (*46*). Here, S_0 is the integral area of slow alpha rhythm (~7.5 to 10 Hz) before alcohol intake, and ΔS is calculated by subtracting S_0 from the integral area of slow alpha rhythm recorded at different times after alcohol intake (figs. S32 and S33). Besides, the concentration of breath alcohol was tracked by LSM-based alcohol gas sensors, which reached the peak value after about 2 hours of wine drinking and returned to the normal value after around 8 hours (fig. S34). Notably, the HR and HR variation (HRV) can be determined from the ECG signals recorded by LSM-based electrophysiological sensors (fig. S22). After drinking white wine, the volunteer's HR increased, and his HRV decreased, indicating decreased efficiency of autonomic control (*47*). It needed about 8 hours for his HR and HRV to return to their normal values.

Light-driven soft actuator based on laser-scribed MoO_2

Soft actuator is the basic building block of some emerging complex functional devices and can find broad applications in reconfigurable 3D structures, reshapable bioelectronics, soft robots, responsive metamaterials, tunable optics, and many others (*12*, *48*). In this section, we have developed LSM-based light-driven soft actuators (Fig. 5 and figs. S35 to S38) by taking advantage of its outstanding photothermal effect (*19*, *20*). As shown in Fig. 5A, the soft actuator consists of PI, LSM, and PDMS trilayer structures. Here, LSM serves as a pliable photothermal heater. Upon infrared illumination (Phillips, BR40 Infrared Lamp), the actuator can bend to the PI side because of the stress caused by the significant thermal expansion difference between PI and PDMS. The maximum bending angle can be controlled by the power density of the infrared lamp (Fig. 5B and fig. S36). The soft actuator takes about 7 s to bend from 0° to 225° and needs about 9 s to recover. Figure 5 (C to F), fig. S37, and movie S2 illustrate reconfigurable 3D structures made of LSM-based soft actuators. The demonstration examples include flower-like 3D structures and windmill-like 3D structures and integrations with mechanically assembled 3D structures (*49*, *50*) to form complicated, multilayer 3D architectures. The reconfigurations between 2D and 3D shapes can be achieved reversibly by turning off and on the infrared illumination. Taking advantage of the 2D-to-3D reconfiguration, a reshapable wearable airflow sensor has been developed (Fig. 5, G and H). The sensor consists of six petal-like LSM-based soft actuators, and each of them is integrated with a strain gauge made of LIG, classified as six sensing channels. These sensing channels are separately addressable. When not in use, the sensor is in its 2D configuration to save space. During operation, the sensor reconfigures into 3D structure, which can not only provide high sensitivity (fig. S38) but also detect the direction of airflow by measuring resistance changes in the six sensing channels. Furthermore, we have developed an LSM-based worm-like smart soft robot (Fig. 5I and movie S3). The smart soft robotic worm, integrated with the ammonia sensor, can perform controlled motions driven through turning on and off the infrared illumination and can detect ammonia leakage in the environment, indicating potential applications in environmental monitoring and homeland security.

DISCUSSION

In summary, we report a laser-assisted, universal fabrication approach to scribing MoO_2 with arbitrary patterns on soft elastomers and other substrates. LSM demonstrates high electrical conductivity, biocompatibility, chemical stability, MRI compatibility, and photothermal effects. Furthermore, we have developed LSM-based on-skin wearable devices that have the Janus device layouts and can link with mobile data acquisition circuits for in situ data processing, wireless data transmission, and graphic data display on the smartphone. The obtained Janus on-skin wearables can not only monitor a rich variety of physiological signals from human skin but also collect useful information from both human breath and surrounding environments. In addition, we have developed an LSM-based light-driven soft actuator and demonstrated its applications in reconfigurable 3D architectures, reshapable wearable airflow meters, and smart soft robotic worms integrated with bioelectronics.

MATERIALS AND METHODS

Materials

Molybdenum chloride, ethanol, phosphate-buffered saline (PBS), ammonium hydroxide, aniline, carbon ink (E3449), and Ag/AgCl ink (E2414) were purchased from Thermo Fisher Scientific. Lactate, UA, glucose, CAF, putrescine, cadaverine, glucose oxidase, iron(III) *p*-toluene sulfonate hexahydrate, and graphite flakes were purchased from Sigma-Aldrich. ZnO nanowires (NWZO01A5) were purchased from ACS Material. PDMS (Sylgard 184) was purchased from Dow. PI (Kapton 100HN) was received from Dupont. SEBS (H1062) was received from Asahi Kasei. Nafion solutions and WSe_2 were purchased from Alfa Aesar.

LSM and device fabrication

The fabrication of LSM begins with the preparation of the precursor solutions [1 M $MoCl_5$ in deionized water (DI water) and ethanol with the volume ratio of 1:4]. Next, the precursor is spray-coated on the targeted substrate using a commercial airbrush (G222; Master Airbrush). Here, the amount of spray-coated $MoCl_5$ can be controlled by the volume of spray-coated precursor solutions. Subsequently, CO_2 laser scribing of MoO_2 is performed using a VLS2.30 universal laser system (wavelength, 10.6 μm; beam size, 120 μm; pulse duration,14 μs; maximum power, 30 W; maximum scanning speed, 23 inches s^{-1}) under ambient conditions. If not particularly indicated, then the setting of the CO_2 laser system is fixed at 7% of the

maximum power, 15% of the maximum scanning speed, a raster mode, 5 for the image density, and 1000 for the pulse per inch. Here, 15% of the maximum laser scanning speed is chosen on the basis of the balance between the production efficiency and production stability. Five for the image density means 500 lines per inch for our CO_2 laser system (VLS2.30). Last, washing away unexposed precursors using DI water and drying the samples in air complete the LSM fabrication process. In addition, porous SEBS was prepared following our published procedures (*25*).

There were no additional modifications on LSM patterns for electrophysiological sensors and temperature sensors. For sweat sensors (fig. S15), carbon ink– and Ag/AgCl ink–modified LSM electrodes were used as the UA/CAF-sensing electrode and reference electrode, respectively. The glucose-sensing electrode was prepared by functionalizing the carbon ink–modified LSM electrode with Au nanoparticles, Prussian blue, and glucose oxidase following our previously published procedures (*51*). The UV sensor, humidity sensor, alcohol gas sensor, and NH_3 gas sensor were prepared by adding 30 μl of ZnO nanowire solution (3 mg ml^{-1} in DI water), 30 μl of GO (3.75 mg ml^{-1} in DI water), 50 μl of WSe_2 solution (10 mg ml^{-1} in 0.5% Nafion solution), and 30 μl of PTS-PANI solution (3 mg ml^{-1} in DI water) onto LSM interdigital electrodes, respectively. Here, GO and PTS-PANI were prepared following the published procedures (*44*, *52*). The soft actuator was prepared by first making LSM on PI (25 μm in thickness), followed by coating of PDMS (~250 μm in thickness) on LSM. Then, CO_2 laser was used to cut samples into predesigned shapes for 3D reconfigurations. For laser cutting, the setting of the CO_2 laser system was fixed at 100% of the maximum power, 100% of the maximum scanning speed, a vector mode, 5 for the image density, and 1000 for the pulse per inch.

Characterizations and measurements

XRD patterns were taken using a Philips X'Pert Materials Research diffractometer equipped with a Cu Kα radiation source. Raman spectra were obtained on a Renishaw Raman microscope. SEM and TEM images were taken with a FEI Quanta 600F Environmental SEM and FEI Tecnai F30 G2 Twin Transmission Electron Microscope, respectively. EDS data were obtained by a Bruker Quantax 200 EDS. Fourier transform infrared (FT-IR) and UV-VIS spectra were collected using a Nicolet 4700 FT-IR spectrophotometer and UV-VIS spectrophotometer (UV-2401, Shimadzu), respectively. Fluorescence images were taken with a Zeiss Axiovert 40 CFL trinocular inverted fluorescence phase contrast microscope. Magnetic susceptibility of LSM was measured by a superconducting quantum interference device (MPMS3, Quantum Design North America, USA). A 3T Siemens Prisma scanner with a 20-channel head coil was used for MRI scanning. Infrared images were collected using a commercial thermal camera (FLIR E6). Mechanical properties were characterized on a Mark-10 ESM303 tensile tester.

For mobile data acquisition, the alcohol, temperature, UV, and NH_3 were detected by monitoring the resistance changes under specific voltages with a source meter module, consisting of a dc/ac generator, an output buffer, and a multiplexer. Humidity was detected by capacitance measurement with the source meter module. The differential pulse voltammetry module was used for UA and CAF monitoring, and chronoamperometry was used for glucose monitoring. Electrophysiological signals were recorded by the physiological potentiometric module consisting of the programmable gain amplifier and digital filter. The signals were smoothed by a low-pass filter and converted by the analog-to-digital converter for further processing in the digital signal processor. The processed data were transmitted to the smartphone wirelessly by Bluetooth Low Energy. The mobile data acquisition circuit was connected to LSM-based wearable devices using the flexible flat cable (Premo-Flex, Molex) and the *Z*-axis conductive tape (Adafruit).

Temperature measurements were validated and calibrated using thermocouples (SA1-K, OMEGA Engineering) with a thermometer (HH309A, OMEGA Engineering). Humidity measurements were validated and calibrated using a traceable hygrometer (Thermo Fisher Scientific). Electrophysiological measurements were validated and conducted using PowerLab T26 (AD Instruments), and electrical stimulations were performed using the same instrument. UV light was produced by a commercial UV light source with (AI-2UV20DC), and the UV intensity was determined by a UV meter (UV513AB, General Tools; 280 to 400 nm). Alcohol measurements were validated and calibrated by a breath alcohol tester (BT-S80, BACtrack). Electrochemical characterizations were conducted using an electrochemical station (CHI660E, CH Instruments Inc.) The airflow rates were measured using a digital anemometer (BT-856-A, BTMETER). The resistance, impedance, and capacitance were measured with an LCR meter (IM3523, HIOKI) and dual-channel source meter (2604B, Keithley Instruments).

In vitro cytotoxicity assay

The cytotoxicity of LSM was studied following a contact mode protocol using HaCaT, U937, and HDF-α (*53*). The LSM samples were cut into disks with a diameter of 1 cm and sterilized with 70% ethanol, followed by rinsing with sterilized PBS. Cells (5×10^4 cells cm^{-2}) were cultured in a 24-well culture plate using Dulbecco's modified Eagle's medium (Thermo Fisher Scientific) supplemented with 10% fetal bovine serum (Thermo Fisher Scientific). After 6 hours for cell attachment on the culturing plate, the presterilized LSM samples were carefully transferred to the wells containing cells, ensuring the samples to contact with the cells. Then, the plate containing both cells and LSM samples was cultured for 5 days, and the culture medium was changed every 2 days. On days 1, 3, and 5, the viability of the cells contacting with LSM samples was determined both qualitatively and quantitatively using an Alamar Blue assay (Thermo Fisher Scientific) and a LIVE/DEAD assay. The Alamar Blue assay was implemented following the protocol provided by the manufacturer. The cells were also stained with a LIVE/DEAD cell viability kit (Thermo Fisher Scientific) and then examined using an inverted fluorescence microscope (Zeiss, White Plains, NY, USA).

Experiments on human participants

All experiments were conducted under approval from the Institutional Review Board at the University of Missouri at Columbia (number 2010272). All human participants gave written and informed consent before participation in the studies.

SUPPLEMENTARY MATERIALS

Supplementary material for this article is available at https://science.org/doi/10.1126/sciadv.abp9734

REFERENCES AND NOTES

1. J. Lin, Z. Peng, Y. Liu, F. Ruiz-Zepeda, R. Ye, E. L. G. Samuel, M. J. Yacaman, B. I. Yakobson, J. M. Tour, Laser-induced porous graphene films from commercial polymers. *Nat. Commun.* **5**, 5714 (2014).

2. K. W. Tan, B. Jung, J. G. Werner, E. R. Rhoades, M. O. Thompson, U. Wiesner, Transient laser heating induced hierarchical porous structures from block copolymer-directed self-assembly. *Science* **349**, 54–58 (2015).
3. W. Gao, N. Singh, L. Song, Z. Liu, A. L. M. Reddy, L. Ci, R. Vajtai, Q. Zhang, B. Wei, P. A. Ajayan, Direct laser writing of micro-supercapacitors on hydrated graphite oxide films. *Nat. Nanotechnol.* **6**, 496–500 (2011).
4. M. F. El-Kady, V. Strong, S. Dubin, R. B. Kaner, Laser scribing of high-performance and flexible graphene-based electrochemical capacitors. *Science* **335**, 1326–1330 (2012).
5. X. Zang, C. Jian, T. Zhu, Z. Fan, W. Wang, M. Wei, B. Li, M. F. Diaz, P. Ashby, Z. Lu, Y. Chu, Z. Wang, X. Ding, Y. Xie, J. Chen, J. N. Hohman, M. Sanghadasa, J. C. Grossman, L. Lin, Laser-sculptured ultrathin transition metal carbide layers for energy storage and energy harvesting applications. *Nat. Commun.* **10**, 3112 (2019).
6. R. Ye, D. K. James, J. M. Tour, Laser-induced graphene: From discovery to translation. *Adv. Mater.* **31**, 1803621 (2019).
7. R. You, Y. Q. Liu, Y. L. Hao, D. D. Han, Y. L. Zhang, Z. You, Laser fabrication of graphene-based flexible electronics. *Adv. Mater.* **32**, 1901981 (2020).
8. Y. Xu, Q. Fei, M. Page, G. Zhao, Y. Ling, D. Chen, Z. Yan, Laser-induced graphene for bioelectronics and soft actuators. *Nano Res* **14**, 3033–3050 (2021).
9. Y. Yang, Y. Song, X. Bo, J. Min, O. S. Pak, L. Zhu, M. Wang, J. Tu, A. Kogan, H. Zhang, T. K. Hsiai, Z. Li, W. Gao, A laser-engraved wearable sensor for sensitive detection of uric acid and tyrosine in sweat. *Nat. Biotechnol.* **38**, 217–224 (2020).
10. D. H. Kim, N. Lu, R. Ma, Y. S. Kim, R. H. Kim, S. Wang, J. Wu, S. M. Won, H. Tao, A. Islam, K. J. Yu, T. I. Kim, R. Chowdhury, M. Ying, L. Xu, M. Li, H. J. Chung, H. Keum, M. Mccormick, P. Liu, Y. W. Zhang, F. G. Omenetto, Y. Huang, T. Coleman, J. A. Rogers, Epidermal electronics. *Science* **333**, 838–843 (2011).
11. D. C. Kim, H. J. Shim, W. Lee, J. H. Koo, D. H. Kim, Material-based approaches for the fabrication of stretchable electronics. *Adv. Mater.* **32**, 1902743 (2020).
12. Y. Ling, W. Pang, X. Li, S. Goswami, Z. Xu, D. Stroman, Y. Liu, Q. Fei, Y. Xu, G. Zhao, B. Sun, J. Xie, G. Huang, Y. Zhang, Z. Yan, Laser-induced graphene for electrothermally controlled, mechanically guided, 3D assembly and human-soft actuators interaction. *Adv. Mater.* **32**, 1908475 (2020).
13. B. Sun, R. N. McCay, S. Goswami, Y. Xu, C. Zhang, Y. Ling, J. Lin, Z. Yan, Gas-permeable, multifunctional on-skin electronics based on laser-induced porous graphene and sugar-templated elastomer sponges. *Adv. Mater.* **30**, 1804327 (2018).
14. Y. Gao, Q. Li, R. Wu, J. Sha, Y. Lu, F. Xuan, Laser direct writing of ultrahigh sensitive SiC-based strain sensor arrays on elastomer toward electronic skins. *Adv. Funct. Mater.* **29**, 1806786 (2019).
15. V. Nair, J. Yi, D. Isheim, M. Rotenberg, L. Meng, F. Shi, X. Chen, X. Gao, A. Prominski, Y. Jiang, J. Yue, C. T. Gallagher, D. N. Seidman, B. Tian, Laser writing of nitrogen-doped silicon carbide for biological modulation. *Sci. Adv.* **6**, eaaz2743 (2020).
16. D. B. Rogers, R. D. Shannon, A. W. Sleight, J. L. Gillson, Crystal chemistry of metal dioxides with rutile-related structures. *Inorg. Chem.* **8**, 841–849 (1969).
17. T. Lüdtke, D. Wiedemann, I. Efthimiopoulos, N. Becker, S. Seidel, O. Janka, R. Pöttgen, R. Dronskowski, M. Koch-Müller, M. Lerch, HP-MoO_2: A high-pressure polymorph of molybdenum dioxide. *Inorg. Chem.* **56**, 2321–2327 (2017).
18. K. Dou, W. Zhu, Y. Zou, Y. Gu, J. Li, S. Zhang, Z. Liu, H. Zeng, Metallic oxide nanocrystals with near-infrared plasmon resonance for efficient, stable and biocompatible photothermal cancer therapy. *J. Mater. Chem. B* **5**, 7393–7402 (2017).
19. Y. Zhan, Y. Liu, H. Zu, Y. Guo, S. Wu, H. Yang, Z. Liu, B. Lei, J. Zhuang, X. Zhang, D. Huang, C. Hu, Phase-controlled synthesis of molybdenum oxide nanoparticles for surface enhanced Raman scattering and photothermal therapy. *Nanoscale* **10**, 5997–6004 (2018).
20. C. Hao, C. Wei, Y. Wang, Z. Sun, H. Liu, R. Dai, M. Huang, S. He, W. Liu, C. Zhu, Thermal/near-infrared light dual-responsive reversible two-way shape memory cEVA/2D-MoO_2 composite for multifunctional applications. *Macromol. Rapid Commun.* **42**, 2100056 (2021).
21. Y. Shi, B. Guo, S. A. Corr, Q. Shi, Y. S. Hu, K. R. Heier, L. Chen, R. Seshadri, G. D. Stucky, Ordered mesoporous metallic MoO_2 materials with highly reversible lithium storage capacity. *Nano Lett.* **9**, 4215–4220 (2009).
22. Y. Jin, H. Wang, J. Li, X. Yue, Y. Han, P. K. Shen, Y. Cui, Porous MoO_2 nanosheets as non-noble bifunctional electrocatalysts for overall water splitting. *Adv. Mater.* **28**, 3785–3790 (2016).
23. Q. Zhang, X. Li, Q. Ma, Q. Zhang, H. Bai, W. Yi, J. Liu, J. Han, G. Xi, A metallic molybdenum dioxide with high stability for surface enhanced Raman spectroscopy. *Nat. Commun.* **8**, 14903 (2017).
24. C. K. N. Patel, Continuous-wave laser action on vibrational-rotational transitions of CO_2. *Phys. Rev.* **136**, A1187–A1193 (1964).
25. Y. Xu, B. Sun, Y. Ling, Q. Fei, Z. Chen, X. Li, P. Guo, N. Jeon, S. Goswami, Y. Liao, S. Ding, Q. Yu, J. Lin, G. Huang, Z. Yan, Multiscale porous elastomer substrates for multifunctional on-skin electronics with passive-cooling capabilities. *Proc. Natl. Acad. Sci. U.S.A.* **117**, 205–213 (2020).
26. B. Hu, L. Mai, W. Chen, F. Yang, From MoO_3 nanobelts to MoO_2 nanorods: Structure transformation and electrical transport. *ACS Nano* **3**, 478–482 (2009).
27. Y. Chyan, R. Ye, Y. Li, S. P. Singh, C. J. Arnusch, J. M. Tour, Laser-induced graphene by multiple lasing: Toward electronics on cloth, paper, and food. *ACS Nano* **12**, 2176–2183 (2018).
28. L. Tian, B. Zimmerman, A. Akhtar, K. J. Yu, M. Moore, J. Wu, R. J. Larsen, J. W. Lee, J. Li, Y. Liu, B. Metzger, S. Qu, X. Guo, K. E. Mathewson, J. A. Fan, J. Cornman, M. Fatina, Z. Xie, Y. Ma, J. Zhang, Y. Zhang, F. Dolcos, M. Fabiani, G. Gratton, T. Bretl, L. J. Hargrove, P. V. Braun, Y. Huang, J. A. Rogers, Large-area MRI-compatible epidermal electronic interfaces for prosthetic control and cognitive monitoring. *Nat. Biomed. Eng.* **3**, 194–205 (2019).
29. N. Driscoll, B. Erickson, B. B. Murphy, A. G. Richardson, G. Robbins, N. V. Apollo, G. Mentzelopoulos, T. Mathis, K. Hantanasirisakul, P. Bagga, S. E. Gullbrand, M. Sergison, R. Reddy, J. A. Wolf, H. I. Chen, T. H. Lucas, T. R. Dillingham, K. A. Davis, Y. Gogotsi, J. D. Medaglia, F. Vitale, MXene-infused bioelectronic interfaces for multiscale electrophysiology and stimulation. *Sci. Transl. Med.* **13**, eabf8629 (2021).
30. J. F. Schenck, The role of magnetic susceptibility in magnetic resonance imaging: MRI magnetic compatibility of the first and second kinds. *Med. Phys.* **23**, 815–850 (1996).
31. K. Muraleedharan, C. K. Subramaniam, N. Venkataramani, T. K. G. Rao, C. M. Srivastava, V. Sankaranarayanan, R. Srinivasan, On the magnetic susceptibility of CuO_x. *Solid State Commun.* **76**, 727–730 (1990).
32. T. R. Ray, J. Choi, A. J. Bandodkar, S. Krishnan, P. Gutruf, L. Tian, R. Ghaffari, J. A. Rogers, Bio-integrated wearable systems: A comprehensive review. *Chem. Rev.* **119**, 5461–5533 (2019).
33. T. Someya, M. Amagai, Toward a new generation of smart skins. *Nat. Biotechnol.* **37**, 382–388 (2019).
34. S. Xu, A. Jayaraman, J. A. Rogers, Skin sensors are the future of health care. *Nature* **571**, 319–321 (2019).
35. L. C. Kloth, Electrical stimulation for wound healing: A review of evidence from in vitro studies, animal experiments, and clinical trials. *Int. J. Low. Extrem. Wounds* **4**, 23–44 (2005).
36. Y. Hosobuchi, J. E. Adams, R. Linchitz, Pain relief by electrical stimulation of the central gray matter in humans and its reversal by naloxone. *Science* **197**, 183–186 (1977).
37. G. Alon, A. F. Levitt, P. A. McCarthy, Functional electrical stimulation enhancement of upper extremity functional recovery during stroke rehabilitation: A pilot study. *Neurorehabil. Neural Repair* **21**, 207–215 (2007).
38. J. Kim, A. S. Campbell, B. E. F. de Ávila, J. Wang, Wearable biosensors for healthcare monitoring. *Nat. Biotechnol.* **37**, 389–406 (2019).
39. M. Bariya, H. Y. Y. Nyein, A. Javey, Wearable sweat sensors. *Nat. Electron.* **1**, 160–171 (2018).
40. K. Kwon, S. Y. Heo, I. Yoo, A. Banks, M. Chan, J. Y. Lee, J. B. Park, J. Kim, J. A. Rogers, Miniaturized, light-adaptive, wireless dosimeters autonomously monitor exposure to electromagnetic radiation. *Sci. Adv.* **5**, eaay2462 (2019).
41. Y. Jin, J. Wang, B. Sun, J. C. Blakesley, N. C. Greenham, Solution-processed ultraviolet photodetectors based on colloidal ZnO nanoparticles. *Nano Lett.* **8**, 1649–1653 (2008).
42. L. Lan, X. Le, H. Dong, J. Xie, Y. Ying, J. Ping, One-step and large-scale fabrication of flexible and wearable humidity sensor based on laser-induced graphene for real-time tracking of plant transpiration at bio-interface. *Biosens. Bioelectron.* **165**, 112360 (2020).
43. W. J. Pan, Y. Zhang, D. Z. Zhang, Self-assembly fabrication of titanium dioxide nanospheres-decorated tungsten diselenide hexagonal nanosheets for ethanol gas sensing application. *Appl. Surf. Sci.* **527**, 146781 (2020).
44. Z. Ma, P. Chen, W. Cheng, K. Yan, L. Pan, Y. Shi, G. Yu, Highly sensitive, printable nanostructured conductive polymer wireless sensor for food spoilage detection. *Nano Lett.* **18**, 4570–4575 (2018).
45. C. Shimamoto, I. Hirata, K. Katsu, Breath and blood ammonia in liver cirrhosis. *Hepatogastroenterology* **47**, 443–445 (2000).
46. S. E. Lukas, J. H. Mendelson, R. A. Benedikt, B. Jones, EEG alpha activity increases during transient episodes of ethanol-induced euphoria. *Pharmacol. Biochem. Behav.* **25**, 889–895 (1986).
47. V. M. Karpyak, M. Romanowicz, J. E. Schmidt, K. A. Lewis, J. M. Bostwick, Characteristics of heart rate variability in alcohol-dependent subjects and nondependent chronic alcohol users. *Alcohol. Clin. Exp. Res.* **38**, 9–26 (2014).
48. S. I. Rich, R. J. Wood, C. Majidi, Untethered soft robotics. *Nat. Electron.* **1**, 102–112 (2018).
49. Z. Yan, F. Zhang, F. Liu, M. Han, D. Ou, Y. Liu, Q. Lin, X. Guo, H. Fu, Z. Xie, M. Gao, Y. Huang, J. H. Kim, Y. Qiu, K. Nan, J. Y. Kim, P. Gutruf, H. Luo, A. Zhao, K. -C. Hwang, Y. Huang, Y. Zhang, J. A. Rogers, Mechanical assembly of complex, 3D mesostructures from releasable multilayers of advanced materials. *Sci. Adv.* **2**, e1601014 (2016).
50. Y. Zhang, Z. Yan, K. Nan, D. Xiao, Y. Liu, H. Luan, H. Fu, X. Wang, Q. Yang, J. Wang, W. Ren, H. Si, F. Liu, L. Yang, H. Li, J. Wang, X. Guo, H. Luo, L. Wang, Y. Huang, J. A. Rogers, A mechanically driven form of Kirigami as a route to 3D mesostructures in micro/nanomembranes. *Proc. Natl. Acad. Sci. U.S.A.* **112**, 11757–11764 (2015).
51. Y. Xu, G. Zhao, L. Zhu, Q. Fei, Z. Zhang, Z. Chen, F. An, Y. Chen, Y. Ling, P. Guo, S. Ding, G. Huang, P. Y. Chen, Q. Cao, Z. Yan, Pencil-paper on-skin electronics. *Proc. Natl. Acad. Sci. U.S.A.* **117**, 18292–18301 (2020).
52. D. C. Marcano, D. V. Kosynkin, J. M. Berlin, A. Sinitskii, Z. Sun, A. Slesarev, L. B. Alemany, W. Lu, J. M. Tour, Improved synthesis of graphene oxide. *ACS Nano* **4**, 4806–4814 (2010).

53. P. Li, Y. F. Poon, W. Li, H.-Y. Zhu, S. H. Yeap, Y. Cao, X. Qi, C. Zhou, M. Lamrani, R. W. Beuerman, E.-T. Kang, Y. Mu, C. M. Li, M. W. Chang, S. S. J. Leong, M. B. Chan-Park, A polycationic antimicrobial and biocompatible hydrogel with microbe membrane suctioning ability. *Nat. Mater.* **10**, 149–156 (2011).
54. S. Maeda, Y. Hara, T. Sakai, R. Yoshida, S. Hashimoto, Self-walking gel. *Adv. Mater.* **19**, 3480–3484 (2007).
55. B. Shin, J. Ha, M. Lee, K. Park, G. H. Park, T. H. Choi, K.-J. Cho, H.-Y. Kim, Hydrobot: A self-locomotive ratcheted actuator powered by enviromental humidity. *Sci. Robot* **3**, eaar2629 (2018).
56. Y. Wang, X. Huang, X. Zhang, Ultrarobust, tough and highly stretchable self-healing materials based on cartilage-inspired noncovalent assembly nanostructure. *Nat. Commun.* **12**, 1291 (2021).
57. J. Mittal, M. Inagaki, Effect of reaction of $MoCl_5$ with atmospheric water on its intercalation into graphite. *Solid State Ion.* **121**, 183–188 (1999).
58. C. Limberg, R. Boese, B. Schiemenz, Intermediates and products of the reaction of $MoCl_5$ with ethanol:crystal structures of $[MoOCl_3(EtOH)]$ and $H[MoOCl_4]\cdot 2EtOH$. *J. Chem. Soc. Dalton Trans.* **9**, 1633–1638 (1997).
59. P. C. H. Mitchell, Oxo-species of molybdenum-(V) and-(VI). *Q. Rev. Chem. Soc.* **20**, 103–118 (1966).
60. S. H. Jeong, S. Zhang, K. Hjort, J. Hilborn, Z. Wu, PDMS-based elastomer tuned soft, stretchable, and sticky for epidermal electronics. *Adv. Mater.* **28**, 5830–5836 (2016).

Acknowledgments

Funding: Z.Y. acknowledges financial support from startup funds and EM Excellence award of the University of Missouri-Columbia and grants from National Science Foundation (award numbers 1917630 and 2045101). J.X. acknowledges financial support from startup funds of the University of Nebraska Medical Center and National Institute of General Medical Science of National Institutes of Health (award numbers R01GM123081 and R01GM138552). **Author contributions:** Z.Y., G.Z., and Y.L. conceived the idea and led research efforts. G.Z., Y.L., Y.S., Zanyu Chen, C.J.M., O.E., A.B., D.R.A., J.H., C.K., Q.C., X.H., D.S., Y.X., Zehua Chen, P.-Y.C., S.G., J.X., and Z.Y. performed the experiments. G.Z. led the design, fabrication, and evaluation of LSM-based biosensors. Y.L. led the design, fabrication, and test of LSM-based soft actuators, reconfigurable 3D structures, and soft robotic worms. Z.Y., G.Z., and Y.L. wrote the manuscript with the assistance of other coauthors. **Competing interests:** The authors declare that they have no competing interests. **Data and materials availability:** All data needed to evaluate the conclusions in the paper are present in the paper and/or the Supplementary Materials.

Submitted 10 March 2022
Accepted 5 May 2022
Published 22 June 2022
10.1126/sciadv.abp9734

ScienceAdvances

Laser-scribed conductive, photoactive transition metal oxide on soft elastomers for Janus on-skin electronics and soft actuators

Ganggang ZhaoYun LingYajuan SuZanyu ChenCherian J. MathaiOgheneobarome EmejeAlexander BrownDinesh Reddy AllaJie HuangChansong KimQian ChenXiaoqing HeDavid StallaYadong XuZehua ChenPai-Yen ChenShubhra GangopadhyayJingwei XieZheng Yan

Sci. Adv., 8 (25), eabp9734. • DOI: 10.1126/sciadv.abp9734

Science Advances (ISSN) is published by the American Association for the Advancement of Science. 1200 New York Avenue NW, Washington, DC 20005. The title *Science Advances* is a registered trademark of AAAS.